Title: The formation of peak rings in large impact craters

Authors: Joanna Morgan[1], Sean Gulick[2], Timothy Bralower[3], Elise Chenot[4], Gail Christeson[2], Philippe Claeys[5], Charles Cockell[6], Gareth S. Collins[1], Marco J. L. Coolen[7], Ludovic Ferrière[8], Catalina Gebhardt[9], Kazuhisa Goto[10], Heather Jones[3], David A. Kring[11], Erwan Le Ber[12], Johanna Lofi[13], Xiao Long[14], Christopher Lowery[2], Claire Mellett[15], Rubén Ocampo-Torres[16], Gordon R. Osinski[17, 18], Ligia Perez-Cruz[19], Annemarie Pickersgill[20], Michael Pölchau[21], Auriol Rae[1], Cornelia Rasmussen[22], Mario Rebolledo-Vieyra[23], Ulrich Riller[24], Honami Sato[25], Douglas R. Schmitt[26], Jan Smit[27], Sonia Tikoo[28], Naotaka Tomioka[29], Jaime Urrutia-Fucugauchi[19], Michael Whalen[30], Axel Wittmann[31], Kosei Yamaguchi[32], William Zylberman[17,33].

Affiliations:

1) Department of Earth Science and Engineering, Imperial College London, SW7 2AZ, UK.

2) Institute for Geophysics, Jackson School of Geosciences, University of Texas at Austin, Texas 78758-4445, USA.

3) Pennsylvania State University, University Park, Pennsylvania 16802, USA.

4) Biogéosciences Laboratory, UMR 6282 CNRS, Université de Bourgogne-Franche Comté, Dijon 21000, France.

5) Analytical, Environmental and Geo-Chemistry , Vrije Universiteit Brussel, Pleinlaan 2,Brussels 1050, Belgium.

6) Centre for Astrobiology, School of Physics and Astronomy, University of Edinburgh, EH9 3FD, UK.

7) Department of Chemistry, Curtin University, Bentley, WA 6102, Australia.

8) Natural History Museum, Burgring 7, 1010 Vienna, Austria.

9) Alfred Wegener Institute Helmholtz Centre of Polar and Marine Research, Bremerhaven, 27568, Germany.

10) Tohoku University, International Research Institute of Disaster Science, Aoba 468-1 E303, Sendai 980-0845, Japan.

11) Lunar and Planetary Institute, 3600 Bay Area Blvd., Houston, TX 77058, USA.

12) Department of Geology, University of Leicester, Leicester, LE1 7RH, UK.

13) Géosciences Montpellier, Université de Montpellier, 34095 Montpellier Cedex05, France.

14) China University of Geosciences (Wuhan), School of Earth Sciences, Planetary Science Institute, 388 Lumo Rd. Hongshan Dist., China.

15) BGS, The Lyell Centre, Research Avenue South, Edinburgh, EH14 4AP, UK.

16) Groupe de Physico-Chimie de l´Atmosphère, ICPEES, UMR 7515 Université de Strasbourg/CNRS 1 rue Blessig, 67000 Strasbourg, France.

17) University of Western Ontario, Centre for Planetary Science and Exploration and Dept. Earth Sciences, London, ON, N6A 5B7, Canada.

18) University of Western Ontario, Dept. Physics and Astronomy, London, ON, N6A 5B7, Canada.

19) Instituto de Geofísica, Universidad Nacional Autónoma de México, Cd. Universitaria, Coyoacán Ciudad de México, C. P. 04510, México.

20) School of Geographical & Earth Sciences, University of Glasgow, Gregory, Lilybank Gardens, Glasgow, G12 8QQ, UK.

21) University of Freiburg, Geology, Albertstraße 23b, Freiburg, 79104, Germany.

22) University of Utah, Department of Geology and Geophysics, 115 S 1460 E (FASB), Salt Lake City, UT 84112, USA.

23) Unidad de Ciencias del Agua, Centro de Investigación, Científica de Yucatán, A.C., Cancún, Quintana Roo, C.P. 77500, México.

24) Institut für Geologie, Universität Hamburg, Bundesstrasse 55, Hamburg, 20146, Germany.

25) Japan Agency for Marine-Earth Science and Technology, 2-15, Natsushima-cho, Yokosuka-city, Kanagawa, 237-0061, Japan.

26) Department of Physics, University of Alberta, Edmonton, Alberta, T6G 2E1,Canada.

27) Vrije Universiteit Amsterdam, Faculty of Earth and Life Sciences FALW de Boelelaan 1085, Amsterdam, 1018HV, Netherlands.

28) Rutgers University New Brunswick, Earth and Planetary Sciences, Piscataway Township, NJ 08854, USA.

29) Kochi Institute for Core Sample Research, Japan Agency for Marine-Earth Science and Technology, 200 Monobe Otsu, Nankoku, Kochi, 783-8502 Japan.

30) University of Alaska Fairbanks, Geosciences, 900 Yukon Dr., Fairbanks, AK 99775, USA.

31) Arizona State University, LeRoy Eyring Center for Solid State Science, Physical Sciences ,Tempe, AZ 85287-1704, USA.

32) Department of Chemistry, Tohu University, Ota-ku Funabashi, Chiba 274-8510, Japan, and NASA Astrobiological Institute.

33) Aix Marseille Univ, CNRS, IRD, Coll France, CEREGE, Aix-en-Provence, France.

One sentence summary: Drilling reveals the lithology and physical state of the Chicxulub peak-ring rocks, and confirms the dynamic collapse model for peak-ring formation.

Abstract:

Large impacts provide a mechanism for resurfacing planets through mixing near-surface rocks with deeper material. Central peaks are formed from the dynamic uplift of rocks during crater formation. As crater size increases, central peaks transition to peak rings. Without samples, debate surrounds the mechanics of peak-ring formation and their depth of origin. Chicxulub is the only known impact structure on Earth with an unequivocal peak ring, but it is buried and only accessible through drilling. Expedition 364 sampled the Chicxulub peak ring, which we found was formed from uplifted, fractured, shocked, felsic basement rocks. The peak-ring rocks are cross-cut by dikes and shear zones and have an unusually low density and seismic velocity. Large impacts therefore generate vertical fluxes and increase porosity in planetary crust.

Main text:

Impacts of asteroids and comets play a major role in planetary evolution by fracturing upper-crustal lithologies, excavating and ejecting material from the impact site, producing melt pools, and uplifting and exposing sub-surface rocks. The uplift of material during impact cratering rejuvenates planetary surfaces with deeper material. Complex impact craters on rocky planetary bodies possess a central peak or a ring of peaks internal to the crater rim, and the craters with these features are termed central-peak and peak-ring craters, respectively (*1*). Most known peak-ring craters occur on planetary bodies other than Earth, prohibiting assessment of their physical state and depth of origin. Here, we address the question of how peak rings are formed using

geophysical data, numerical simulations, and samples of the Chicxulub peak ring obtained in a joint drilling expedition by the International Ocean Discovery Program (IODP) and International Continental Scientific Drilling Program (ICDP).

Upon impact, a transient cavity is initially formed which then collapses to produce a final crater that is both shallower and wider than the transient cavity (*1*). Dynamic uplift of rocks during the collapse of the transient cavity in the early stages of crater formation (Fig. 1B-C) likely forms central peaks (*2*). The dynamic collapse model of peak-ring formation attributes the origin of peak rings to the collapse of over-heightened central peaks (*3*). The observational evidence for this model is most obvious on Venus, where central peaks gradually evolve into peak rings with increasing crater size (*4*). The peak-ring to crater-rim diameter ratio increases with crater size on Venus, but does not get much larger than approximately 0.5. The lack of any further increase in this ratio led to the suggestion that in larger craters the outward collapse of peak ring material is halted when it meets the collapsing transient cavity rim (*4*).

A different concept for peak-ring formation, the nested melt-cavity hypothesis, evolved from observations of peak-ring craters on the Moon and Mercury (*5*-*7*). This alternative hypothesis envisions that the uppermost central uplift is melted during impact, and an attenuated central uplift remains below the impact melt sheet and does not overshoot the crater floor during the modification stage. Hence, in contrast to the dynamic collapse model (Fig. 1), this nested melt-cavity hypothesis would not predict outward thrusting of uplifted rocks above the collapsed transient cavity rim material. The origin and shock state of rocks that form a peak ring are less clear in the nested melt-cavity hypothesis, as they have not been evaluated with numerical

simulations. Head (*6*), however, postulated that material in the outer margin of the melt cavity forms the peak ring and, therefore should be close to melting. This requires shock pressures of just below 60 GPa. In contrast, Baker et al. (*7*) propose that peak rings are formed from inwardly-slumped rotated blocks of transient cavity rim material originating at shallow depths and, thus, should have experienced lower average shock pressures than simulated in the dynamic collapse model.

The transition from central-peak to peak-ring craters with increasing crater size scales inversely with gravity (*1*), suggesting the same transition diameter of about 30 km found on Venus (*4*) should also hold for Earth, and that craters > 30 km in diameter should possess a peak ring. Craters on Earth often display internal ring-like structures, but complications and uncertainties due to target heterogeneity, erosion and sedimentation, make it difficult to distinguish peak rings that are genetically linked to their extraterrestrial counterparts (*8-9*). Seismic reflection data across the ~200-km diameter Chicxulub multi-ring impact structure revealed it to be the only terrestrial crater with an unequivocal and intact peak ring, with the same morphological structure as peak-ring craters on Venus, Mercury, the Moon, and other rocky bodies (*10-14*). These seismic data and previous drilling also revealed a terrace zone formed from slump blocks of Mesozoic sedimentary rocks, with the innermost blocks lying directly underneath or close to the outer edge of the peak ring (Fig. 1G). This observation supported the idea that peak rings in larger craters could be created through the interaction of two collapse regimes with the peak-ring rocks being formed from uplifted crustal basement that had collapsed outward and been emplaced above the collapsed transient cavity rim (*15*).

Numerical shock-physics simulations (e.g. Fig. 1) are consistent with the dynamic collapse model in that they reproduce this mode of peak-ring formation as well as other crater features such as the observed mantle uplift and terrace zone (*16-20*). For the simulation in Figure 1 we used well and geophysical data to construct the pre-impact target, which is comprised of a 33-km thick crust with ~3-km of sedimentary rocks above basement (*21*). We tracked the material that eventually forms the Chicxulub peak ring and show that it originates from mid-crustal basement (8-10 km depth) that is shocked to pressures over 10 GPa (Fig. 1A). The peak-ring rocks first move outward and upward as the initial transient cavity forms (Fig. 1B), then progress inward to form part of the zone of central uplift (Fig. 1C), and finally collapse outward to be emplaced above collapsed transient cavity rim material composed of sedimentary rocks (light grey) that were originally between 0- and 3-km depth (Fig. 1D-F). The dynamic collapse model therefore predicts that the Chicxulub peak ring is formed from uplifted crystalline basement rocks. Structural data from a number of exposed terrestrial impact structures supports the idea of dynamic collapse of the central uplift (*9, 22-24*) and that, in larger craters, the peak ring is formed from the interaction of two collapse regimes (*25*). In the simulation, the final crater (Fig. 1F) has the same key features as the upper 10 km of the Chicxulub crater as imaged on a radial, depth-converted seismic reflection profile (*21*) (Fig. 1G). Specifically, a suite of dipping reflectors mark the boundary between Mesozoic sedimentary rocks and peak-ring rocks, with evidence of discrete melt zones within the peak ring (especially in the upper few hundred meters).

Prior to drilling, not all of the geophysical data appeared to be consistent with the hypothesis that the Chicxulub peak ring was formed from uplifted crustal basement. Gravity models and seismic

refraction data indicated that the peak-ring rocks had a relatively low density (2.2-2.3 g cm^{-3}) (*26*) and seismic P-wave velocity (3.9-4.5 km s^{-1}) (*27*). The seismic velocity of crustal basement rock outside the central crater is > 5.6 km s^{-1} (*28*), making it difficult to explain how crustal rocks within the peak ring could have such a strongly reduced seismic velocity. The inferred physical properties have been explained by the peak ring either being formed from a thickened section of allochthonous impact breccia (*26*) that is a typical cover of crater floors or from megabreccia (allochthonous breccia with large clasts > 10 m) as seen in one of the annular rings at the Popigai impact structure in Siberia (*8*).

In April-May 2016, a joint effort by the IODP and ICDP drilled the Chicxulub peak ring offshore during Expedition 364 at site M0077A (21.45° N, 89.95° W) (Fig. 2A). The drill site is located at ~45.6 km radial distance, using a previously selected nominal center for the Chicxulub structure of 21.30° N, 89.54° W (*10*). We recovered core between 505.7 and 1334.7 meters below the sea floor (mbsf). We made visual descriptions through a transparent liner, while samples from the end of the core barrel (core catcher) were available for direct inspection. We made 114 smear slides and 51 thin sections from the core-catcher samples, which were taken at regular intervals throughout the drill core. We measured petrophysical properties at the surface using a Multi Sensor Core Logger (MSCL), and acquired a suite of wireline logging data from the sea floor to the bottom of the hole (*21*).

The upper part of the cored section from 505 to 618 mbsf consists of a sequence of hemipelagic and pelagic Paleogene sediments. We reached the top of the peak ring at 618 mbsf (Fig. 2A, B). The uppermost peak ring is composed of ~130 m of breccia with impact melt fragments that

overlie clast-poor impact melt rock (Fig. 2B). We encountered felsic basement rocks between 748 and 1334.7 mbsf that were intruded by pre-impact mafic and felsic igneous dikes as well as impact-generated dikes. We recovered one particularly thick impact breccia and impact melt rock sequence between 1250 and 1316 mbsf. The entire section of felsic basement exhibits impact-induced deformation on multiple scales. There are many fractures (Fig. 3A), foliated shear zones (Fig. 3B) and cataclasites (Fig. 3C), as well as signs of localized hydrothermal alteration (Fig. 3D). The felsic basement is predominantly a coarse-grained, roughly-equigranular granitic rock (Fig. 3E), that is locally aplitic or pegmatitic, and in a few cases syenitic. The basement rocks in the peak ring differ from basement in near-by drill holes encountered immediately below the Mesozoic sedimentary rocks, suggesting a source of origin that was deeper than 3 km (*21*).

In total 18 of the smear slides and 17 of the thin sections were prepared from the felsic basement and viewed using an optical microscope. Evidence of shock metamorphism is pervasive throughout the entire basement with quartz crystals displaying up to four sets of decorated planar deformation features (Fig. 3F). We observed shatter cone fragments in pre-impact dikes between 1129 and 1162 mbsf, as well as within the breccia (Fig. 3G). Jointly, the observed shock metamorphic features suggest that the peak ring rocks were subjected to shock pressures of approximately 10 to 35 GPa (*29*). No clear systematic variation in shock metamorphism was observed with depth. We note that impact melt, which is formed at shock pressures of >60 GPa, is also a component of the peak ring (Fig. 2B).

The formation of the Chicxulub peak ring from felsic basement (Fig. 2) confirms that crustal rocks lie directly above Mesozoic sedimentary rocks (Fig. 1G), which is consistent with the dynamic collapse model of peak-ring formation (Fig. 1A-F). On the contrary, the nested melt-cavity hypothesis does not predict this juxtaposition of units at the peak ring. In the numerical simulation shown in Figure 1, the majority of the rocks that form the peak ring are subjected to peak-shock pressures in the 10-35 GPa range, with some zones of melt rock (colored red), which is also consistent with our drill-core observations. Conversely, in the nested melt-cavity hypothesis, the peak-ring rocks are expected to be subjected to either higher (*6*) or lower average shock pressures (*7*) than we observed.

We investigated the physical properties of the peak-ring rocks using: 1) core-based MSCL natural gamma ray (NGR) and gamma density logs; and 2) downhole sonic logs and vertical seismic profile (VSP) data that determine P-wave velocity surrounding the borehole (Fig. 2C)(*21*). The drilling data confirm that the peak-ring rocks have low densities and seismic velocities, as suggested by geophysical models (*26-27*). The density of the felsic basement varies between 2.10 and 2.55 g cm^{-3}, with a mean of 2.41 g cm^{-3}, and P-wave velocities vary between 3.5 and 4.5 km s^{-1}, with a mean of 4.1 km s^{-1}. These values are unusually low for felsic basement, which typically has densities of > 2.6 g cm^{-3} and seismic velocities of > 5.5 km s^{-1}. We found that samples of the peak ring were variable in strength, locally quite hard or friable. We also observed distinct variations in rate of drill bit penetration over short distances (< 1 m), with some sections seeming mechanically weaker than others. Fracturing, shock metamorphism, and other factors, such as hydrothermal alteration, may contribute to the reduction in seismic velocity and density of the felsic basement. Dilation during brittle deformation is observed in

central uplifts in other large terrestrial impact craters (*30-31*), and dilatancy is predicted to increase fracture porosity in the peak-ring rocks by between 1 and 5% (*32*). Shock metamorphism can also reduce density, as shown in experiments (*33*) and in nature (*34*).

One of the most enigmatic and enduring fundamental unknowns in impact cratering is how bowl-shaped transient cavities collapse to form larger, relatively-flat, final craters (*1*). To do so requires a temporary reduction in cohesive strength and internal friction (*35-36*). In the model shown in Figure 1, the rocks in the peak ring have moved a large distance (> 20 km) during crater formation, hence, these units may well provide clues to the transient weakening mechanism that allows large craters to collapse.

The confirmation of the dynamic collapse model (Fig. 1A-F) by the Expedition 364 results provides predictions about shock-deformation, density reduction, and the kinematics of peak-ring formation. These predictions can be tested and refined through drill-core investigations of physical properties, paleomagnetism, structural data, and shock metamorphism. We anticipate improvement in constraints on impact energy and the sizes of the transient and excavation cavities. As a consequence, the volumes of environmental pollutants released by the K-Pg impact will be better constrained, together with its role in causing the end-Cretaceous mass extinction (*37*). As the deep subsurface biosphere is influenced by fracturing and mineralogical changes in host rocks induced by shock and post-impact hydrothermal activity, understanding how impact craters are formed and modify the environment will advance our understanding of deep subsurface life on Earth and potential habitability elsewhere.

The validation of the dynamic collapse model also strengthens confidence in simulations of large-crater formation on other planetary bodies. These simulations suggest that, as crater size increases, the rocks that form peak rings originate from increasingly deeper depths (*38*). This relationship means that the composition of the peak-ring lithology provides information on the crustal composition and layering of planetary bodies, and be used to verify formation models, such as for the Moon (e.g., *6*, *38*-*39*). One of the principal observations used to support a version of the nested melt-cavity hypothesis in Baker et al. (*7*) is that peak rings within basins of all sizes on the Moon contain abundant crystalline anorthosite and must, therefore, originate from the upper crust if indeed the lower crust is noritic. Our results suggest a deeper origin for peak-ring rocks, and thus are more in accordance with alternative models for the composition of a heterogeneous lunar crust in which an anorthositic layer extends regionally to deeper depths (*40*-*41*). The dynamic collapse model and Expedition 364 results predict density reduction by shock and shear fracturing within the uplifted material (*33*), which is consistent with the recent Gravity Recovery and Interior Laboratory (GRAIL) mission results of a highly porous lunar crust (*42*) and the presence of mid-crustal rocks juxtaposed by shear zones in the peak ring at Schrödinger crater (*38*). This linkage between deformation and overturning of material at the scales > 10 km implies that over an extended period of time impact cratering greatly increases the porosity of the subsurface and cause vertical fluxes of materials within the crust.

References

1. H. J. Melosh, *Impact Cratering* (Oxford University Press, NY, 1989).

2. W. S. Hale, R. A. F. Grieve, Volumetric analysis of complex lunar craters: implications for basin ring formation, *J. Geophys. Res*. **87**, A65 (1982).

3. J. B. Murray, Oscillating peak model of basin and crater formation, *Moon and Planets* **22**, 269 (1980).

4. J. S. Alexopoulos, W. B. McKinnon, Large impact craters and basins on Venus with implications for ring mechanics on the terrestrial planets, *Spec. Pap. Geol. Soc. Am*. **293**, 29 (1994).

5. M. J. Cintala, R. A. F. Grieve, Scaling impact melting and crater dimensions: implications for the lunar cratering record. *Meteorit. Planet. Sci*. **33**, 889. doi: 10.1111/j.1945-5100.1998.tb01695.x (1998).

6. J. W. Head, Transition from complex craters to multi-ringed basins on terrestrial planetary bodies: scale-dependent role of the expanding melt cavity and progressive interaction with the displaced zone, *Geophys. Res. Lett*., **37**, L02203 (2010).

7. D. M. H. Baker J. W. Head, G. S. Collins, R. W. K. Potter, The formation of peak-ring basins: working hypothesis and path forward to constrain models of impact-basin formation, *Icarus* **273**, 146 (2016).

8. P. M. Vermeesch, J. V. Morgan, Chicxulub central crater structure: initial results from physical property measurements and combined velocity and gravity modeling, *Meteorit. Planet. Sci.* **39**, 1019 (2004).

9. G. R. Osinski, J. G. Spray, Tectonics of complex crater formation as revealed by the Haughton impact structure, Devon Island, Canadian High Arctic, *Meteorit. Planet. Sci*. **40,** 1813 (2005).

10. A. Camargo-Zanoguera, G. Suarez-Reynoso, Evidencia sismica del crater de impacto de Chicxulub, *Bol. Asoc. Mex. Geof. Expl.* **34**, 1 (1994).

11. J. V. Morgan *et al*., Size and morphology of the Chicxulub impact crater, *Nature* **390**, 471 (1997).

12. A. R. Hildebrand *et al*., Mapping Chicxulub crater structure with gravity and seismic reflection data, *Spec. Pub. Geol. Soc. London* **140**, 177 (1998).

13. S. P. S. Gulick *et al*., Importance of pre-impact crustal structure for the asymmetry of the Chicxulub impact crater, *Nat. Geosci.* **1**, 131 (2008).

14. S. P. S. Gulick, G. L. Christeson, P. J. Barton, R. A. F. Grieve, J. V. Morgan, J. Urrutia-Fucugauchi, Geophysical characterization of the Chicxulub impact crater, *Rev. Geophys.* **51**, 31 (2013).

15. J. Brittan, J. Morgan, M. Warner, L. Marin, Near-surface seismic expression of the Chicxulub impact structure, *Spec. Pap. Geol. Soc. Am*. **339**, 269 (1999).

16. J. V. Morgan, M. R. Warner, G. S. Collins, H. J. Melosh, G. L. Christeson, Peak ring formation in large impact craters. *Earth Planet. Sci. Lett.* **183**, 347 (2000).

17. B. Ivanov, Numerical modeling of the largest terrestrial meteorite craters. *Sol. Syst. Res*. **39**, 381 (2005).

18. G. S. Collins *et al*., Dynamic modeling suggests terrace zone asymmetry in the Chicxulub crater is caused by target heterogeneity, *Earth Planet. Sci. Lett*., **270**, 221 (2008).

19. G. L. Christeson, G. S. Collins, J. V. Morgan, Sean P. S. Gulick, P. J. Barton, M. R. Warner, Mantle deformation beneath the Chicxulub impact crater, *Earth. Planet. Sci. Lett*., **284**, 249 (2009).

20. L. E. Senft, S. T. Stewart, Dynamic fault weakening and the formation of large impact craters, *Earth Planet. Sci. Lett*., **287**, 471 (2009).

21. Materials and Methods are available as Supplementary Materials on Science Online.

22. T. Kenkmann, I. von Dalwigk, Radial transpression ridges: a new structural feature of complex impact craters, *Meteorit. Planet. Sci*. **35**, 1189 (2000).

23. T. Kenkmann, G. S. Collins, K. Wünnemann, The modification stage of impact crater formation, *Impact cratering* (Wiley-Blackwell, 2013) p. 60.

24. A. Jahn, U. Riller, Kinematics of large terrestrial impact crater formation inferred from structural analysis and three-dimensional block modeling of the Vredeford Dome, South Africa, *Geol. Soc. Am. Spec. Pap.* **518**, 85 (2015).

25. R. A. F. Grieve, W. U. Reimold, J. Morgan, U. Riller, M. Pilkington, Observations and interpretations at Vredefort, Sudbury and Chicxulub: Towards an empirical model of terrestrial impact basin formation, *Meteorit. Planet. Sci.* **43**, 855 (2008).

26. M. Pilkington, A. Hildebrand, C. Ortiz-Aleman, Gravity and magnetic field modeling and structure of the Chixculub crater, Mexico, *J. Geophys. Res*. **99**, 13147 (1994).

27. J. V. Morgan *et al*., Full waveform tomographic images of the peak ring at the Chicxulub impact crater, *J. Geophys. Res*. **116**, B06303 (2011).

28. G. Christeson, Y. Nakamura, R. T. Buffler, J. Morgan, M. Warner, Deep crustal structure of the Chicxulub impact crater, *J. Geophys. Res*. **106**, 21751 (2001).

29. R. A. F. Grieve, F. Langenhorst, D. Stöffler, Shock metamorphism of quartz in nature and experiment: II. Significance in geoscience, *Meteorit. Planet. Sci.* **31**, 6 (1996).

30. D. Lieger, U. Riller, R. L. Gibson, Generation of fragment-rich pseudotachylite bodies during central uplift formation in the Vredefort impact structure, *Earth Planet. Sci. Lett*. **279**, 53 (2009).

31. U. Riller, D. Lieger, R. L. Gibson, R. A. F. Grieve, D. Stöffler, Origin of large-volume pseudotachylite in terrestrial impact structures, *Geology* **38**, 619 (2010).

32. G. S. Collins, Numerical simulations of impact crater formation with dilatancy, *J. Geophys. Res.* **119**, 2600 (2014).

33. F. Langenhorst, A. Deutsch, Shock experiments on pre-heated α- and β-quartz: 1. Optical and density data, *Earth Planet. Sci. Lett.* **125**, 407 (1994).

34. A. C. Singleton, G. R. Osinski, P. J. A. McCausland, D. E. Moser, Shock-induced changes in density and porosity in shock-metamorphosed crystalline rocks, Haughton impact structure, Canada, *Meteorit. Planet. Sci.* **46**, 1774 (2011).

35. H. J. Melosh, *Impact and Explosion Cratering* (Pergamon Press, NY, 1977) p. 1245.

36. W. B. McKinnon, An investigation into the role of plastic failure in crater modification, *Lunar Planet. Sci. Conf. Proc*. **9**, 3965 (1978).

37. P. R. Renne *et al*., Time scales of critical events around the Cretaceous-Paleogene boundary, *Science* **339**, 684-687, 10.1126/science.1230492 (2013).

38. D. A. Kring, G. Y. Kramer, G. S. Collins, R, W. K. Potter, M. Chandnani, Peak-ring structure and kinematics from a multi-disciplinary study of the Schrödinger impact basin. *Nature Comm*., in press.

39. G. Y. Kramer, D. A. Kring, A. L. Nahm, C. M. Pieters, Spectral and photogeologic mapping of Schrödinger Basin and implications for post-South Pole-Aitken impact deep subsurface stratigraphy, *Icarus* **223**, 131 (2013).

40. S. Yamamoto *et al*., Massive layer of pure anorthosite on the Moon, *Geophys Res. Lett*. **39**, L13201 (2012).

41. T. Arai, H. Takeda, A. Yamaguchi, M Ohtake, A new model of lunar crust: asymmetry in crustal composition and evolution, *Earth Planets Space* **60**, 433 (2008).

42. M. A. Wieczorek *et al*., The crust of the Moon as seen by GRAIL, *Science* **339**, 671 (2013).

43. K. Wünnemann, A strain-based porosity model for use in hydrocode simulations of impacts

and implications for transient crater growth in porous targets, *Icarus* **180**, 514, doi:10.1016/j.icarus.2005.10.013 (2006).

44. G. S. Collins et al., iSALE-Dellen manual. Figshare 136 pages. doi:10.6084/m9.figshare.3473690 (2016).

45. A. A. Amsden, H. M. Ruppel, C. W. Hirt, SALE: Simplified ALE Computer Program for Fluid Flow at all Speeds (LA-8095). Los Alamos National Laboratory, Los Alamos, NM. (1980).

46. H. J. Melosh, E. V. Ryan, E. Asphaug, Dynamic Fragmentation in Impacts: Hydrocode Simulation of Laboratory Impacts. *J. Geophys. Res.* **97***,* 14735 (1992).

47. B.A Ivanov, D. Deniem, G. Neukum,. Implementation of dynamic strength models into 2D hydrocodes: Applications for atmospheric breakup and impact cratering, International Journal of Impact Engineering, Hypervelocity Impact Proceedings of the 1996 Symposium **20**, 411. doi:10.1016/S0734-743X(97)87511-2 **(**1997**).**

48. G. S. Collins, H. J. Melosh, B. A. Ivanov, Modeling damage and deformation in impact simulations, *Meteorit. Planet. Sci*. **39**, 217. doi:10.1111/j.1945-5100.2004.tb00337.x (2004).

49**.** E. Lopez Ramos, Geological summary of the Yucatan peninsula, In: The Ocean Basins and Margins, vol. 3, The Gulf of Mexico and the Caribbean, A.E.M. Nairn and F.G. Stehli, Eds., Plenum, New York, 257 (1975).

50. J. Urrutia-Fucugauchi, A. Camargi-Zanoguera, L. Perez-Cruz, G. Perez-Cruz, The Chicxulub multi-ring impact crater, Yucatan carbonate platform, Gulf of Mexico, *Geofísica Internacional* **50-1**, 99(2011)**.**

51. C. Bell, J. V. Morgan, G. J. Hampson, B. Trudgill, Stratigraphic and sedimentological observations from seismic data across the Chicxulub impact basin, *Meteorit. Planet. Sci*. **39**, 1089 (2004).

52. Britt, D.T., Yeomans, D., Housen, K., Consolmagno, G., 2002. Asteroid Density, Porosity, and Structure, in: Asteroids III, W. F. Bottke Jr., A. Cellino, P. Paolicchi, and R. P. Binzel (eds), University of Arizona Press, Tucson, p.485-500.

53. E. Pierazzo, D. A. Kring, H. J. Melosh, Hydrocode simulation of the Chicxulub impact event and the production of climatically active gases, *J. Geophys. Res.* **103**, 28607. doi:10.1029/98JE02496 (1998).

54. E. Pierazzo, A. M. Vickery, H. J. Melosh, H.J. A Reevaluation of Impact Melt Production, *Icarus* **127**, 408 (1997).

55. W. Benz, A. G. W. Cameron, H. J.Melosh, The origin of the Moon and the single-impact hypothesis III. *Icarus* **81**, 113. doi:10.1016/0019-1035(89)90129-2 (1989).

56. Thompson, S.L., Lauson, H.S., 1972. Improvements in the Chart D radiation-hydrodynamic CODE III: Revised analytic equation of state (No. SC-RR--71-0714). Sandia National Laboratories, Albuquerque, N. Mex., USA.

57. B.A. Ivanov, H. J. Melosh, E. Pierazzo, Basin-forming impacts: Reconnaissance modeling, *Geological Society of America Special Papers* **465**, 29. doi:10.1130/2010.2465(03) (2010).

58. H. J. Melosh, B. A. Ivanov, Impact Crater Collapse, Annual Reviews in Earth and Planetary *Science* **27**, 385 (1999).

59. H. J Melosh, Acoustic fluidization: A new geologic process? *Journal of Geophysical Research: Solid Earth* **84**, 7513. doi:10.1029/JB084iB13p075131979.

60. K. Wünnemann, B. A. Ivanov, Numerical modelling of the impact crater depth–diameter dependence in an acoustically fluidized target, *Planetary and Space Science* **51**, 831. doi:10.1016/j.pss.2003.08.0012003 (2003).

61. Arculus et al., http://publications.iodp.org/proceedings/351/EXP_REPT/CHAPTERS/351_102.PDF (2015), p23-24

62. D. R. Schmitt, In situ seismic measurements in borehole LB-08A in the Bosumtwi impact structure, Ghana: Preliminary interpretation, *Meteorit. Planet. Sci*. **42**, 755 (2007).

63. K. Wünnemann, G. S. Collins, G. R. Osinski, Numerical modelling of impact melt production in porous rocks, *Earth Planet. Sci. Lett.* **269**, 530. doi:10.1016/j.epsl.2008.03.007 (2008).

Acknowledgments: This research used samples and data provided by the International Ocean Discovery Program. Samples can be requested at: http://web.iodp.tamu.edu/sdrm/ after the end of the moratorium on 19th October 2017. Expedition 364 was jointly funded by the European Consortium for Ocean Research Drilling (ECORD) and the International Continental Scientific Program, with contributions and logistical support from the Yucatan State Government and Universidad Nacional Autónoma de México (UNAM).

Fig. 1. Dynamic collapse model of peak-ring formation. (A-F) Numerical simulation of the formation of Chicxulub (*18*) at: 0, 1, 3, 4, 5, and 10 minutes tracking the material that eventually forms the peak ring (indicated by the arrow in A), and records the maximum shock pressure (blue color scale) to which the peak-ring rocks were exposed during passage of the shock wave.

The red color indicates zones of impact melt, for which shock pressures have exceeded 60 GPa. The pre-impact target rocks are composed of sediments (light gray), crust (medium gray), and mantle (dark gray). (G) Depth-converted, time-migrated seismic profile ChicxR3 (*13*). ChicxR3 is a radial profile (roughly west-northwest) that passes ~200 m from the location of M0077A. For comparison with the simulation, shading is added to match the final crater shown in (F), with light gray for inward-collapsed sedimentary rock, dark gray for peak-ring material, and white for Cenozoic sedimentary cover (*21)*. Black dashed lines indicate dipping reflectors at the outer boundary of the peak ring and red dashed lines mark reflectors that may be consistent with zones of impact melt rock in (F). IODP/ICDP Site M0077A is shown in (G) and placed in a similar position on the magnified inset of the model in (F). VE = vertical exaggeration.

Fig. 2. IODP/ICDP Expedition 364. (A) Location of Site M0077A on depth-converted seismic reflection profile ChicxR3 (*13,14*), overlain by seismic P-wave velocity (*27*). (B) Lithology encountered at Site M0077A from 600 m to total depth, with Paleogene sediments (gray), breccia with impact melt fragments (blue), impact melt rock (green), felsic basement (pink), and pre-impact dikes (yellow). In order to indicate a possible difference in origin, the blue and green color within the breccia is slightly lighter than in the dikes. (C) Corresponding petrophysical properties: gamma density (g/cc) and natural gamma ray (NGR)(cps) measured on the cores using an MSCL, and seismic P-wave velocity (km/s) obtained from sonic (red) and VSP (blue) wireline logging data (*21*).

Fig. 3. Photographs from Expedition 364. Felsic basement displaying: (A) brittle faulting at 749.5 mbsf; (B) a foliated shear zone at 963.5 mbsf; (C) a cataclastic shear zone at 957.4 mbsf;

(D) hydrothermal alteration at 930 mbsf; and (E) typical granitic basement with large crystals of red/brown potassium feldspar at 862.3 mbsf. (F) shocked quartz from 826.9 mbsf in cross-polarised light, displaying three sets of planar deformation features (indicated by the solid white bars). (G) Shatter cone fragment from an amphibolite clast in the breccia at 708.5 mbsf.

Supplementary Materials:

Material and Methods

Table S1

References 43-63.

Figure 1

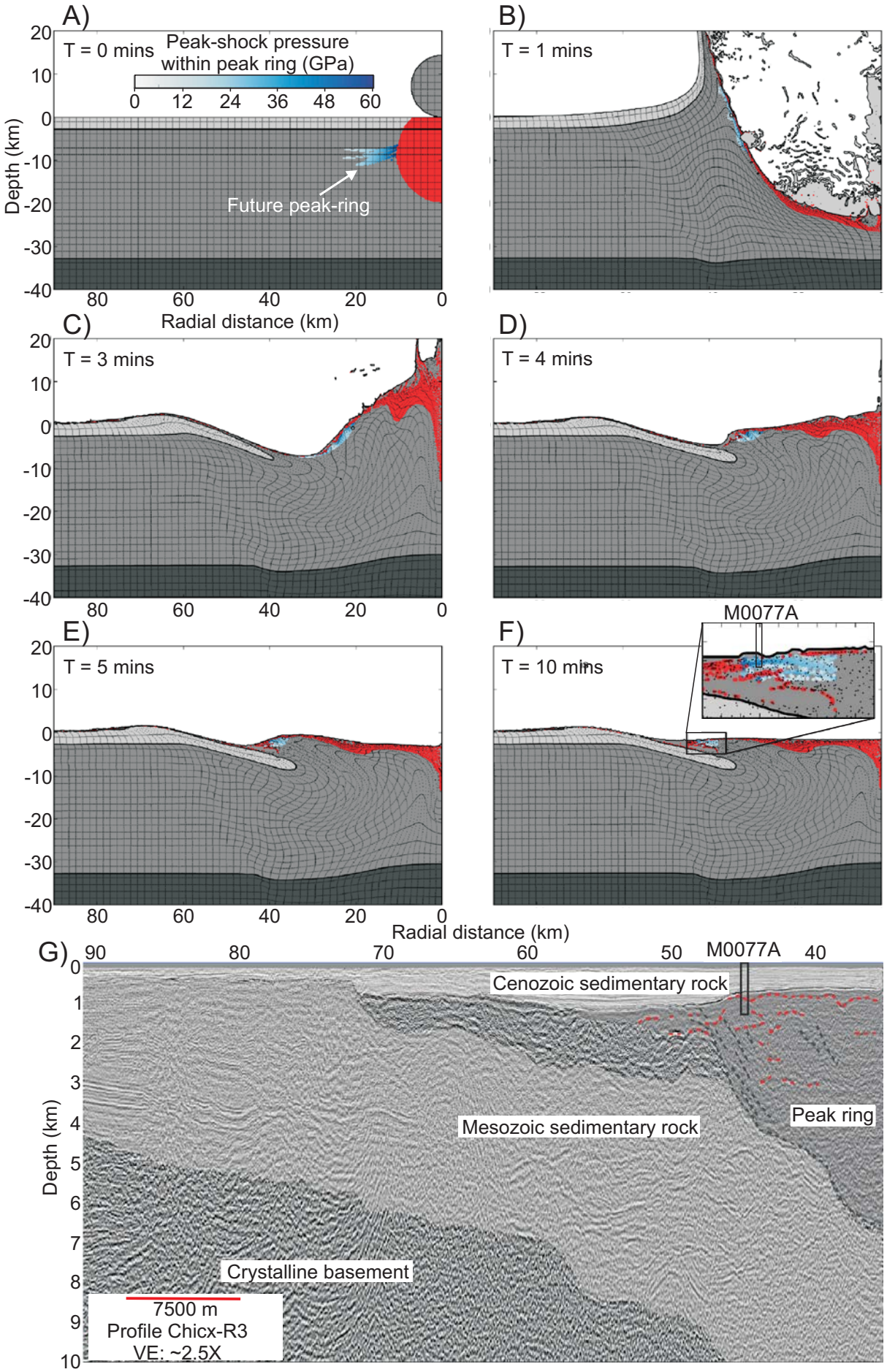
A)
T = 0 mins
Peak-shock pressure within peak ring (GPa)
0 12 24 36 48 60
Future peak-ring
Depth (km)
Radial distance (km)
B)
T = 1 mins
C)
T = 3 mins
D)
T = 4 mins
E)
T = 5 mins
F)
T = 10 mins
M0077A
Radial distance (km)
G)
M0077A
Cenozoic sedimentary rock
Mesozoic sedimentary rock
Peak ring
Crystalline basement
7500 m
Profile Chicx-R3
VE: ~2.5X
Depth (km)

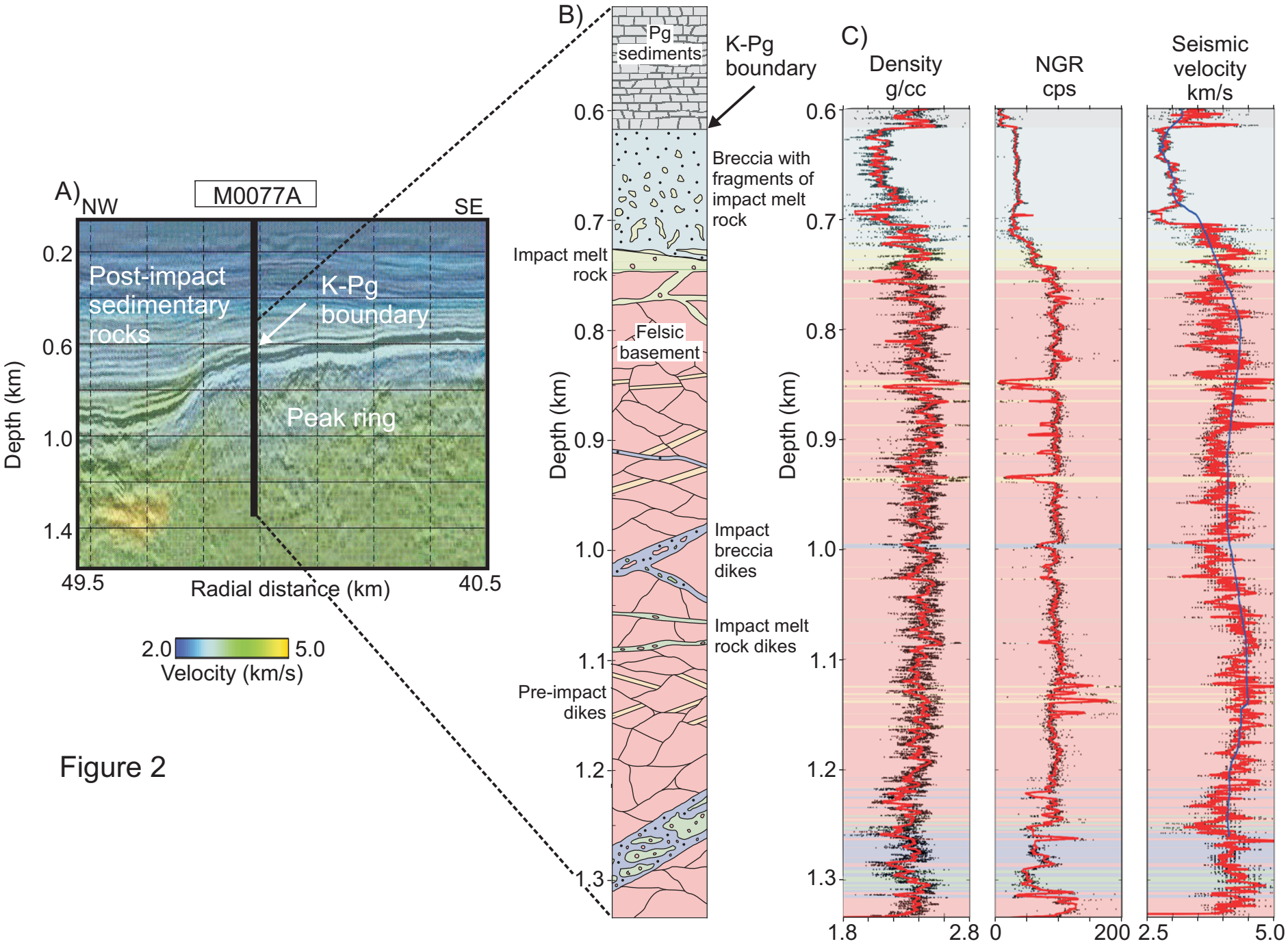
A)
NW
M0077A
SE
Post-impact sedimentary rocks
K-Pg boundary
Peak ring
Depth (km)
0.2
0.6
1.0
1.4
49.5
Radial distance (km)
40.5
2.0
5.0
Velocity (km/s)
B)
Pg sediments
K-Pg boundary
Breccia with fragments of impact melt rock
Impact melt rock
Felsic basement
Impact breccia dikes
Impact melt rock dikes
Pre-impact dikes
Depth (km)
0.6
0.7
0.8
0.9
1.0
1.1
1.2
1.3
C)
Density g/cc
NGR cps
Seismic velocity km/s
1.8
2.8
0
200
2.5
5.0

Figure 2

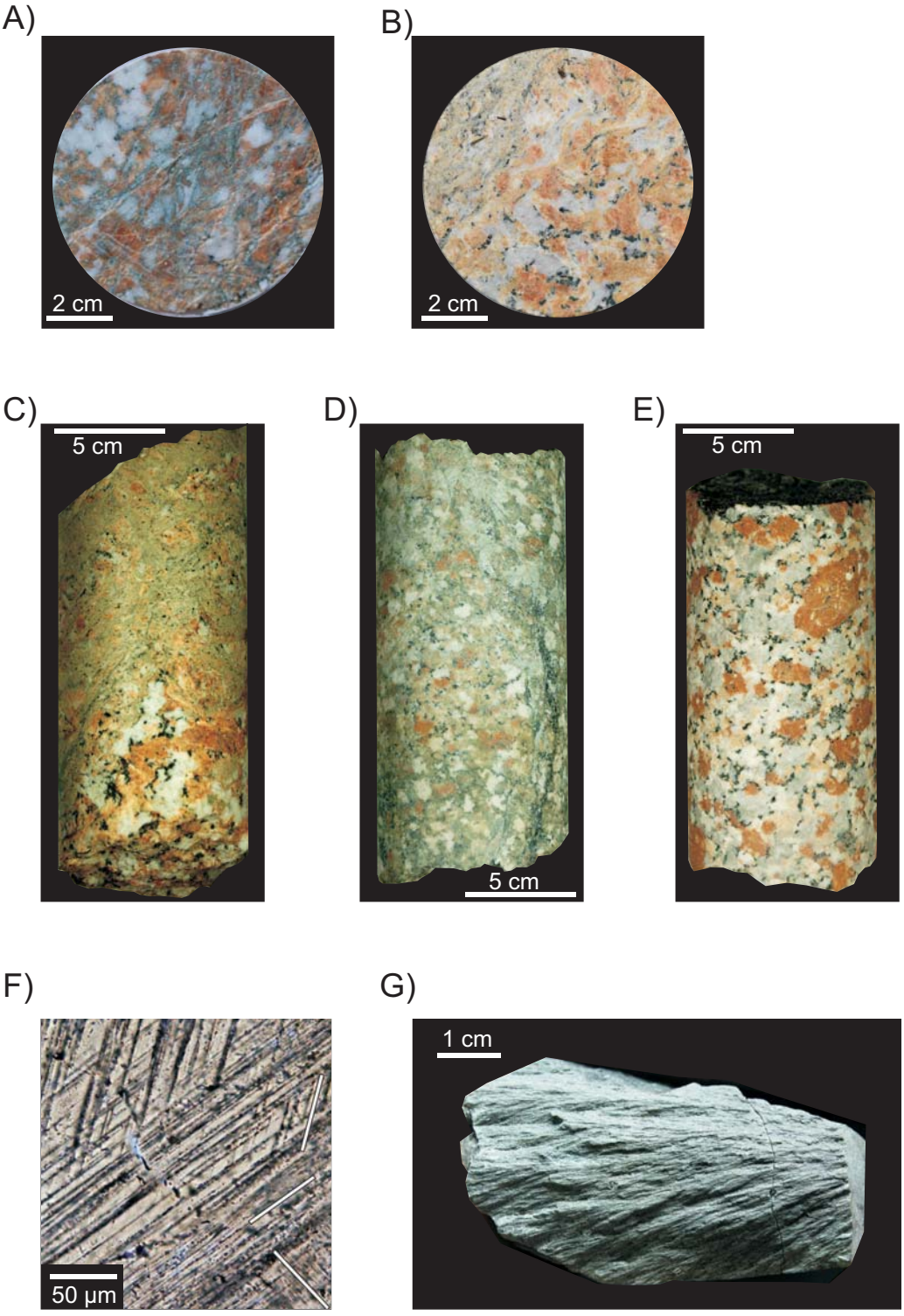

Figure 3